Highly efficient (BiO)$_2$CO$_3$-BiO$_{2-x}$-graphene photocatalysts: Z-Scheme photocatalytic mechanism for their enhanced photocatalytic removal of NO

Yuefa Jia[a,b], Shiping Li[a], Jianzhi Gao[a], Gangqiang Zhu[a,*], Fuchun Zhang[c], Xianjin Shi[d], Yu Huang[d], Chunli Liu[b,*]

[a] School of Physics and Information Technology, Shaanxi Normal University, Xi'an, 710062, PR China
[b] Department of Physics and Oxide Research Center, Hankuk University of Foreign Studies, Yongin, 17035, Republic of Korea
[c] College of Physics and Electronic Information, Yan'an University, Yan'an, 716000, PR China
[d] State Key Lab of Loess and Quaternary Geology (SKLLQG), Institute of Earth Environment, Chinese Academy of Sciences, Xi'an, 710061, PR China

ARTICLE INFO

ABSTRACT

NO removal is one of the most important issues in dealing with air pollution. In this report, Z-scheme (BiO)$_2$CO$_3$-BiO$_{2-x}$-graphene (BOC-BiO$_{2-x}$-GR) composite photocatalyst was designed for NO removal under simulated solar light irradiation. Characterizations of physical properties of the ternary composites revealed extended light absorption and high efficient electron-hole separation. Through the optimization of the BiO$_{2-x}$ content, we observed that the BOC-BiO$_{2-x}$(35wt%)-GR composite exhibited superior photocatalytic activities in NO removal as compared to pure BOC, BiO$_{2-x}$, and BOC-BiO$_{2-x}$ binary composites. Detailed microstructural observation showed that the BOC-BiO$_{2-x}$ heterojunction was formed between BOC (013) and BiO$_{2-x}$ (111) planes. The density of state (DOS) calculation revealed that due to the different hybridization conditions in the energy bands of BOC and BiO$_{2-x}$, the Z-scheme charge transfer should be dominant at the heterojunction interface. The density functional theory (DFT) computation on the Fermi level results confirmed that energy band structure between BOC and BiO$_{2-x}$ is more in favor of the transfer of photo-generated electrons from CB of BOC to the VB of BiO$_{2-x}$, which can be further enhanced by highly conductive GR sheets. The electron spin resonance (ESR) experiments results show that O$_2{}^{\cdot-}$ and HO$^{\cdot}$ were produced during the photocatalytic process, which further provided evidences that the BOC-BiO$_{2-x}$(35wt%)-GR composite works as a Z-scheme photocatalyst. This work indicates that Bi-based nanomaterials can be employed as a stable and high efficient solar light active photocatalyst for NO removal in air pollution control.

1. Introduction

Nitric oxide (NO) have been a primary cause of acid rain, smog and solid particles PM2.5, which lead to a wide variety of negative impact on human health especially respiratory diseases [1,2]. It is important to find efficient and economical ways to remove NO from the atmosphere. Currently, many established techniques and methods have been explored for NO removal. The commonly adopted NO control technologies include wet scrubbing [3], biofiltration [4], thermal catalytic reduction [5], and selected catalytic reduction [6], but these methods are uneconomical and inefficient for the removal of NO at the parts per billion (ppb) level [7,8]. Regarding this issue, semiconductor photocatalysts, which is considered a promising approach for NO removal at ppb levels, have received much interest because of their eco-friendly merit and high photocatalyst efficiency [9]. Research on semiconductor photocatalysts for NO purification was initially focused on TiO$_2$ because of its low cost, non-toxicity, and high activity. Because the UV light occupies only around 5% of solar light as compared to the visible light (52%), the efficiency of TiO$_2$ is mainly limited by its relatively larger band gap energy (~3.2 eV) [10]. Besides TiO$_2$, several novel photocatalysts, including Bi-based materials [11,12], g-C$_3$N$_4$-based materials [13], perovskite LaFeO$_3$-SrTiO$_3$ composite [8], graphene-decorated 3D BiVO$_4$ [14], and Bi$_2$MoO$_6$ [2] have also been reported for their favorable photocatalytic activities in the removal of NO at low concentration.

(BiO)$_2$CO$_3$ (BOC), as an emerging Bi-based semiconductor, has attracted special attention due to its low mammalian toxicity and good photocatalytic capability [15]. However, as a photocatalyst, BOC can only absorb UV light and exhibit a poor photo-generated electron-hole (e^--h^+) pairs separation ability [16,17]. Great efforts have been

---

* Corresponding authors.
E-mail addresses: zgq2006@snnu.edu.cn (G. Zhu), chunliliu@hufs.ac.kr (C. Liu).

devoted to overcome these drawbacks and maximize its photocatalytic activity. For instance, fabricating of type-II heterojunctions (e.g., $Bi_2O_3/(BiO)_2CO_3$ [15] and $g-C_3N_4/(BiO)_2CO_3$ [18]), p-n heterojunctions(e.g., $(BiO)_2CO_3/ZnFe_2O_4$ [19]), and Z-scheme heterojunctions (e.g., $(BiO)_2CO_3/MoS_2$ [20] and $(BiO)_2CO_3/MoS_2$ on carbon nanofibers [21]) can greatly improve the catalytic performance of BOC. Among these hybrid composites, the Z-scheme systems composed of two or more semiconductors are promising photocatalysts for efficient NO removal due to their advantages in promoting the spatial separation of photoinduced charges and keeping the reduction and the oxidation reactions at two different materials. For instance, BOC-based Z-scheme systems such as $AgI/Ag/I-(BiO)_2CO_3$ [22], $(BiO)_2CO_3/MoS_2$ [20], and $(BiO)_2CO_3/MoS_2$ on carbon nanofibers [21] have been designed and showed enhanced photocatalytic activities for dye or NO degradation. Therefore, it is still desirable to fabricate high active and stable BOC-based Z-scheme photocatalysts for the elimination of NO.

BiO_{2-x} is a narrow band gap ($< 2 eV$) semiconductor with good visible light response (up to 850 nm) [23–25]. Due to these advantages, BiO_{2-x} has been investigated as a highly efficient photocatalyst for pollutant degradation or bacterial inactivation under visible light irradiation [23–25]. We considered the $BOC-BiO_{2-x}$ nanocomposites because the former is an emergent attractive photocatalyst for NO and the latter is a good visible light and near-infrared light (NIR) response oxidative semiconductor [20–23]. The E_{CB} and E_{VB} of BiO_{2-x} are about $-0.55 eV$ and $0.85 eV$ [23], whereas those of BOC are about $+0.2 eV$ and $3.53 eV$ [26]. Considering the band edge positions of BiO_{2-x} and BOC, it is possible to realize a Z-sheme phototcatalyst system using these two materials. Therefore, the photogenerated electrons can transfer from the CB of BOC to the VB of the BiO_{2-x} and recombine with the holes there. In this case, most electrons in BiO_{2-x} and holes in BOC participate in the reduction and oxidation reactions, respectively, resulting in an improved photocatalytic NO removal efficiency in the Z-scheme $BOC-BiO_{2-x}$ catalyst.

Furthermore, to ensure the above proposed Z-scheme charge transfer to occur, a good interfacial conductivity is necessary. Since the electrical conductivity of BOC is not good [27], Graphene (GR) has been chosen as the charge transfer bridge for preparing Z-scheme $BOC-BiO_{2-x}$ photocatalysts due to its outstanding high electron conductivity [28,29]. Although BOC/GR or BOC/rGO nanocomposites have been reported for photocatalyst applications [30,31], the $BOC-BiO_{2-x}-GR$ composite has not been prepared and investigated as an all-solid-state Z-scheme photocatalyst.

In this work, we report for the first time the synthesis of $BOC-BiO_{2-x}-GR$ ternary Z-Scheme photocatalyst. The photocatalytic study revealed that $BOC-BiO_{2-x}-GR$ showed much higher NO removal capability than BOC or BOC-GR. In addition, the photochemical stability was confirmed and the separation mechanism of photogenerated $e^- - h^+$ in the Z-Scheme photocatalyst was elucidated through the surface photovoltage spectroscopy (SPV), 5,5-di-methyl-*1*-pyrroline Noxide- electronic spin resonance (DMPO-ESR), first principle density functional theory (DFT) simulations, and the band edge position estimation.

2. Experiment section

2.1. Synthesis of BOC

The BOC nanoparticles were synthesized using a hydrothermal method. Typically, sodium citrate (1.2 g) and $Bi(NO_3)_3·5H_2O$ (5.82 g) were first dissolved in 60 mL HNO_3 (1 M) in a 100 mL autoclaved Teflon vessel and then stirred for 60 min A suitable amount of aqueous NaOH (~1.6 M) was added to the above solution to maintain the pH value of the solution at 5.4, and the resulting solution was further stirred for 60 min. The resulting precursor suspension was hydrothermally treated at 180°C for 24 h. The final products were washed using ethanol for several times and dried in air at 70°C for 12 h to obtain BOC.

2.2. Synthesis of BiO_{2-x}

BiO_{2-x} was prepared by the hydrothermal method. Firstly, $NaBiO_3·2H_2O$(1.68 g) was dispersed in 30 mL of deionized water. Then, 20 mL NaOH solution (1.6 M) was added to the above suspension. The suspension was transferred into a 100 ml autoclaved Teflon vessel and maintained at 180°C for 6 h. After cooling to room temperature, BiO_{2-x} was collected and washed with deionized water for five times, and dried at 70°C.

2.3. Synthesis of $BOC-BiO_{2-x}$

To prepare the $BOC-BiO_{2-x}$ composite, an appropriate amount of BOC and BiO_{2-x} were firstly completely dispersed in 50 mL deionized water and stirred for 30 min. And then the mixed solution was sonicated for 30 min and transferred into a 100 mL Teflon-lined autoclave which was maintained at 180°C for 12 h. After cooling to room temperature, the $BOC-BiO_{2-x}$ composite was obtained by drying at 70°C. The mass ratio of BiO_{2-x}/BOC is designed as 5%, 15%, 25%, 35%, and 45%. Accordingly, the obtained sample was denoted as $BOC-BiO_{2-x}$(5 wt%), $BOC-BiO_{2-x}$(15 wt%), $BOC-BiO_{2-x}$(25 wt%), $BOC-BiO_{2-x}$(35 wt%), and $BOC-BiO_{2-x}$(45 wt%), respectively.

2.4. Synthesis of $BOC-BiO_{2-x}$(35 wt%)-GR

0.13 g of BOC, 0.07 g of BiO_{2-x}, and 35 mg GR (Graphene nanoplatelets, > 99.5% purity, thickness: 4–20 nm, diameter size: 5–10 μm, less than 20 layers, Aladdin Chemistry Co., Ltd, Shanghai, China) were added into 60 mL of absolute ethanol and stirred for 1 h. The mixed solution was then sonicated for 30 min and transferred into a 100 mL Teflon-lined autoclave which was maintained at 180°C for 12 h. The resulting sample was collected by centrifugation, washed by deionized water, and dried in air 70°C for 12 h. The sample was labeled as $BOC-BiO_{2-x}$(35 wt%)-GR.

The detailed of characterization, photocatalytic measurement, in situ FTIR investigation on photocatalytic NO oxidation, and electronic structure calculation can be found in Supporting Information.

3. Results and discussion

3.1. Characterization of $BOC-BiO_{2-x}$(35 wt%)-GR

Fig. 1a presents the XRD diffraction patterns of BOC, BiO_{2-x}, $BOC-BiO_{2-x}$ with different BiO_{2-x} weight percentages, and $BOC-BiO_{2-x}$(35 wt%)-GR. The peaks observed with BOC can be assigned to the characteristic peaks of standard card of $(BiO)_2CO_3$ (PDF# 41-1488, Fig. S1). The XRD patterns of $BOC-BiO_{2-x}$ obviously consisted of two sets of diffraction peaks. Besides to the peaks of the BOC, there were five sharp diffraction peaks at 2θ values of 28.2°, 32.7°, 46.9°, 55.6° and 58.9°, which could be indexed to the (111), (200), (220), (311), and (222) crystal planes of BiO_{2-x} (PDF#47-1057, Fig. S1), respectively. The diffraction peaks intensity of BiO_{2-x} was enhanced with the increased BiO_{2-x} content, which further confirmed the co-existence of BOC and BiO_{2-x} in the $BOC-BiO_{2-x}$ nanocomposite. Due to the small weight ratio of GR in the prepared composite, no diffraction peak from GR was observed [29]. Meanwhile, no characteristic peak from other impurity phase was detected in the synthesized samples, indicating the successful synthesis of high-purity $BOC-BiO_{2-x}$(35 wt%)-GR nanocomposites.

The UV–vis DRS of the all samples are shown in Fig. 1b. Pure BOC exhibited a stronger absorption in the UV region, whereas BiO_{2-x} displayed a much strong absorption in the visible and NIR light region with an absorption edge of about 850 nm. Both $BOC-BiO_{2-x}$(35 wt%) and $BOC-BiO_{2-x}$(35 wt%)-GR composites exhibit boosted visible light absorption. This phenomenon demonstrates that coupling BiO_{2-x} with BOC can effectively enhance the visible light harvesting efficiency, which in turn will be beneficial for the photocatalysis. The plots
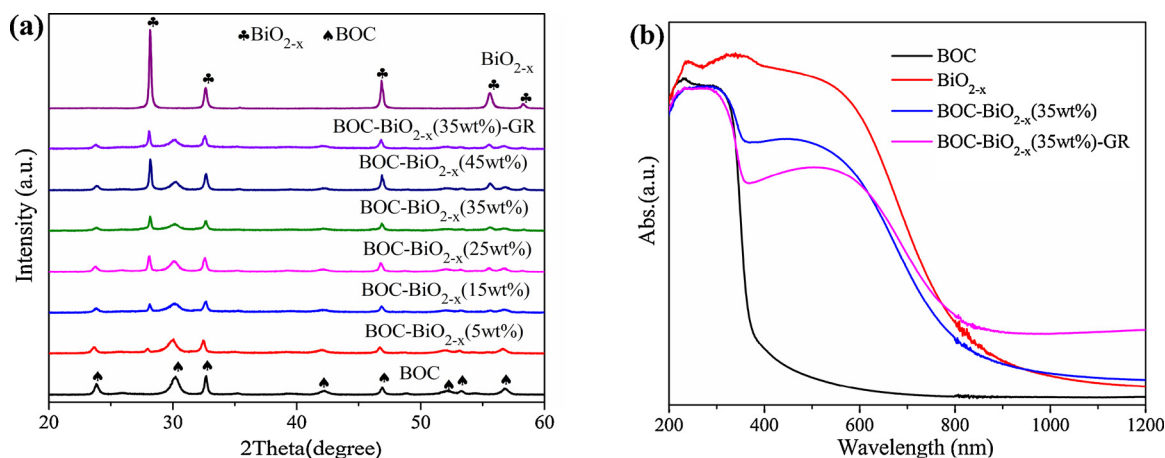
Fig. 1. (a) XRD of all samples and (b) UV–vis DRS of BOC, BiO_{2-x}, BiO_{2-x}-BiO_{2-x}(35 wt%) and BOC-BiO_{2-x}(35 wt%)-GR.

obtained via the transformation based on the Kubelka-Munk function *vs* the photon energy is shown in Fig. S2. The estimated band-gap values were about 3.45, 1.68, 2.98, and 3.20 eV for BOC, BiO_{2-x}, BOC-BiO_{2-x}(35 wt%), and BOC-BiO_{2-x}(35 wt%)-GR, respectively. The band gap of BOC-BiO_{2-x}(35 wt%) and BOC-BiO_{2-x}(35 wt%)-GR was reduced remarkably as compared with BOC. Since it has been reported that the introduction of GR has little effect on the band gap of BOC, the narrowed band gap of BOC-BiO_{2-x}(35 wt%) and BOC-BiO_{2-x}(35 wt%)-GR can be mainly attributed to the BiO_{2-x} introducing. Overall, the UV–vis characterization confirmed the improved optical absorption property of the BOC-BiO_{2-x}(35 wt%) and BOC-BiO_{2-x}(35 wt%)-GR composites.

Fig. 2a shows a comparison of the Raman spectra from GR, BOC, BiO_{2-x}, BOC-BiO_{2-x}(35 wt%) and BOC-BiO_{2-x}(35 wt%)-GR. GR showed two strong peaks at 1350 and 1600 cm^{-1} corresponding to the well-documented D band and G band [28], respectively. The intensity of D band was stronger than that of G band, implying the presence of high density of defects and structure disorder in GR. As for the BOC-BiO_{2-x}(35 wt%) and BOC-BiO_{2-x}(35 wt%)-GR composites, several characteristic bands at 162 cm^{-1} and 355 cm^{-1} can be attributed to the external vibration of BOC [30]. The band at 1070 cm^{-1} was assigned to CO_3^{2-}, and the other peaks at 312 cm^{-1} and 478 cm^{-1} were ascribed to BiO_{2-x} [23,30]. Fig. 2b is the enlarged view of the Raman spectra of BOC-BiO_{2-x}(35 wt%)-GR around 1400 cm^{-1}, where peaks at 1355 cm^{-1} and 1589 cm^{-1} can be observed due to the D band and G band of GR [32,33], respectively. Therefore, the Raman spectra also confirmed the co-existence of BOC, BiO_{2-x} and GR in the BOC-BiO_{2-x}(35 wt%)-GR composite.

The surface chemical composition of the pure BiO_{2-x}, BOC-BiO_{2-x}(35 wt%) and BOC-BiO_{2-x}(35 wt%)-GR samples were investigated by XPS (Fig. 3 and Fig. S3). Fig. 3a shows the survey of BOC-BiO_{2-x}(35 wt%) and BOC-BiO_{2-x}(35 wt%)-GR, indicating that C, Bi, and O existed on the surface of those samples without other elements detected. Especially, the intensity of C1s peaks in BOC-BiO_{2-x}(35 wt%)-GR was higher than that of BOC-BiO_{2-x}(35 wt%), which may be attributed to the introduction of GR. This observation is consistent with the Raman spectra analysis. The C1s spectrum of BOC-BiO_{2-x}(35 wt%)-GR composite was shown in Fig. 3b, it can be deconvoluted into four distinct peaks at 284.6 eV for C=C/C−C/C−H, 285.3 eV for C−OH, 286.2 eV for C−O−C/C=O and 289.6 eV for COOH, respectively [34]. In the high resolution XPS spectrum of Bi4f peaks (Fig. 3c), the XPS peaks of $Bi4f_{7/2}$ and $Bi4f_{5/2}$ of BiO_{2-x} were at 159.7 and 165.2 eV, and $Bi4f_{7/2}$ and $Bi4f_{5/2}$ of BOC were at 160.6 and 165.8 eV [35], respectively, which are the features of Bi(III) and Bi(V) in BOC-BiO_{2-x}(35 wt%)-GR. It was calculated that the ratio between Bi(III) and Bi(V) on the surface of pure BiO_{2-x} is 1.38 (Fig. S3). So the x value in BiO_{2-x} is 0.1 and the as-prepared BOC-BiO_{2-x}(35 wt%)-GR can be written as BOC-$BiO_{1.9}$(35 wt%)-GR. The binding energies of O1s at 530.7, 531.6 and 532.3 eV were associated with lattice oxygen, chemical adsorbed oxygen and oxygen vacancy (Fig. 3d), respectively [23,34].

The morphology and structure of the obtained samples were investigated by SEM as shown in Fig. 4a–d. Fig. 4a displayed the SEM images of BOC, in which the BOC sample are completely made up of flower-like micro-spheres with a nearly uniform size of ca. 2–4 μm in diameter. The enlarged views of as-prepared BOC further reveal that
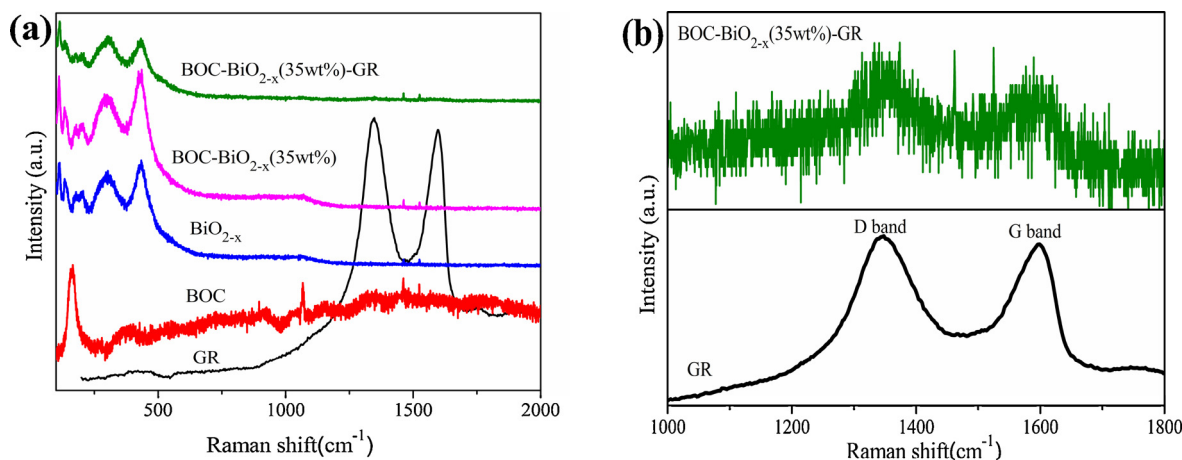

Fig. 2. (a) Raman spectra of GR, BOC, BiO_{2-x}, BiO_{2-x}-BiO_{2-x}(35 wt%) and BOC-BiO_{2-x}(35 wt%)-GR, (b) enlarged view of the Raman spectra of GR and BOC-BiO_{2-x}(35 wt%)-GR.
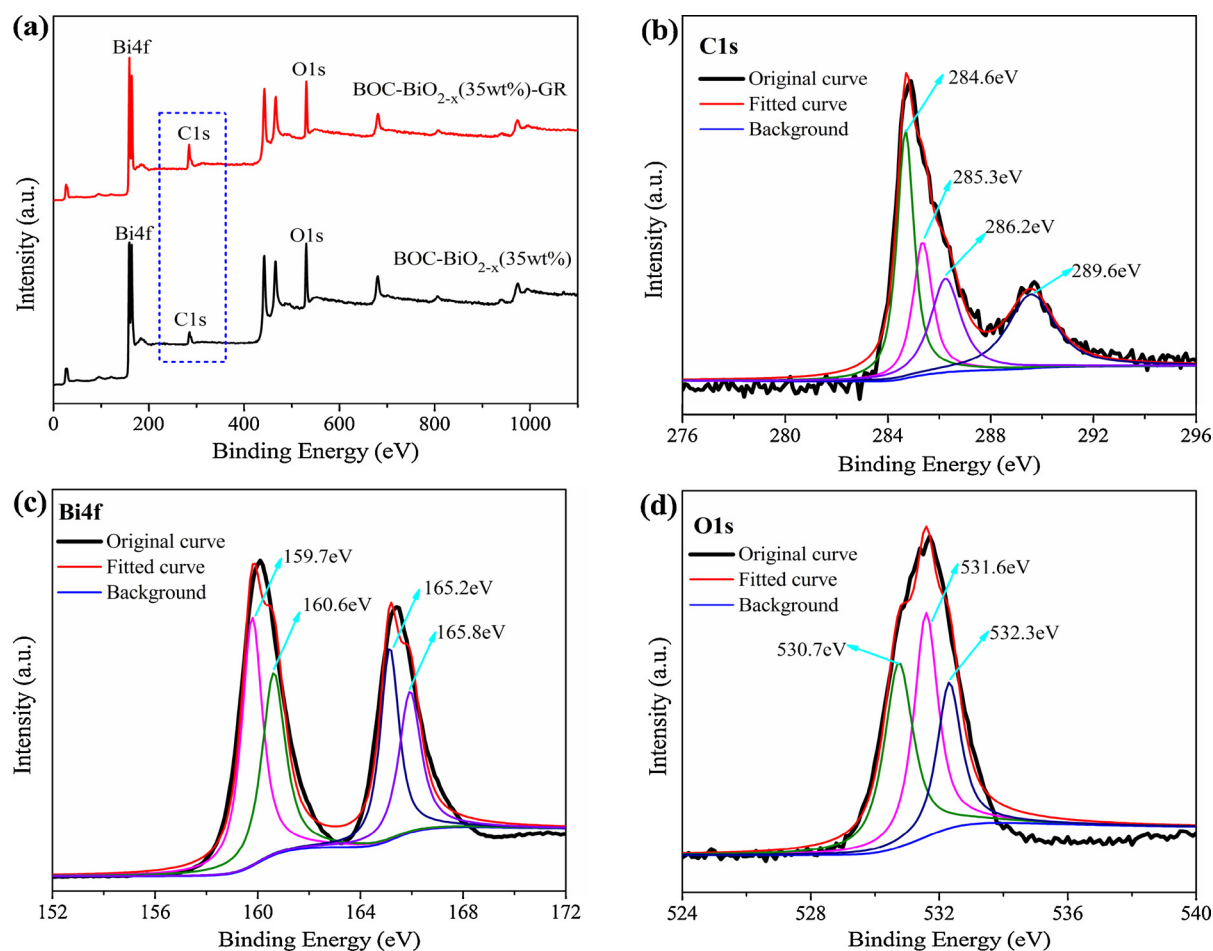
Fig. 3. (a) XPS spectra of BOC-BiO$_{2-x}$(35 wt%) and BOC-BiO$_{2-x}$(35 wt%)-GR, high-resolution XPS spectra of (b) C1s, (c) Bi4f and (d) O1s of BOC-BiO$_{2-x}$(35 wt%)-GR.
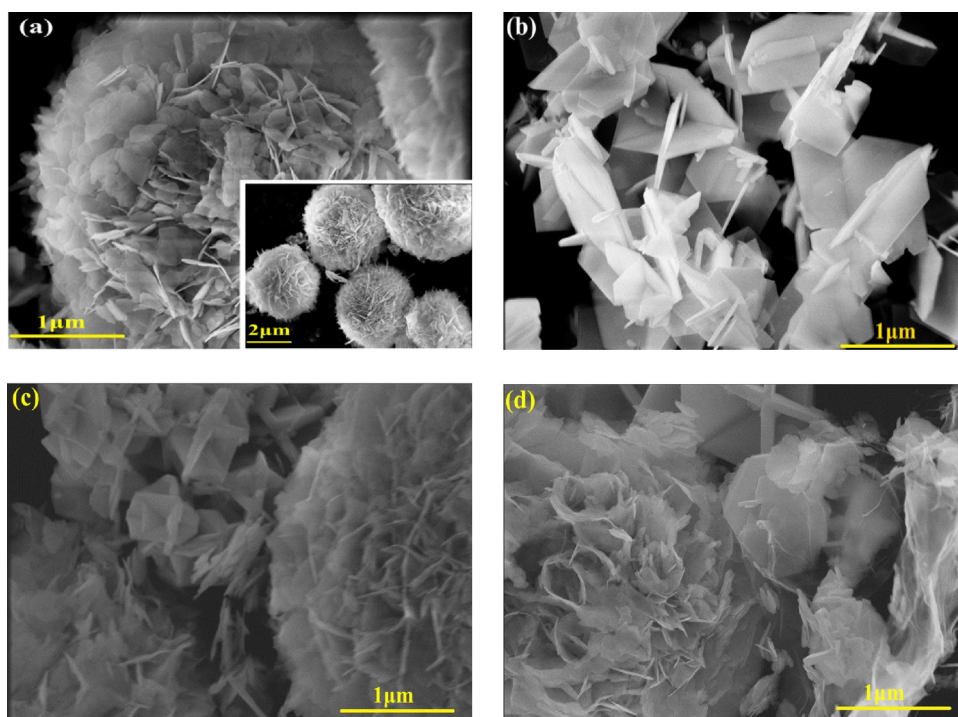

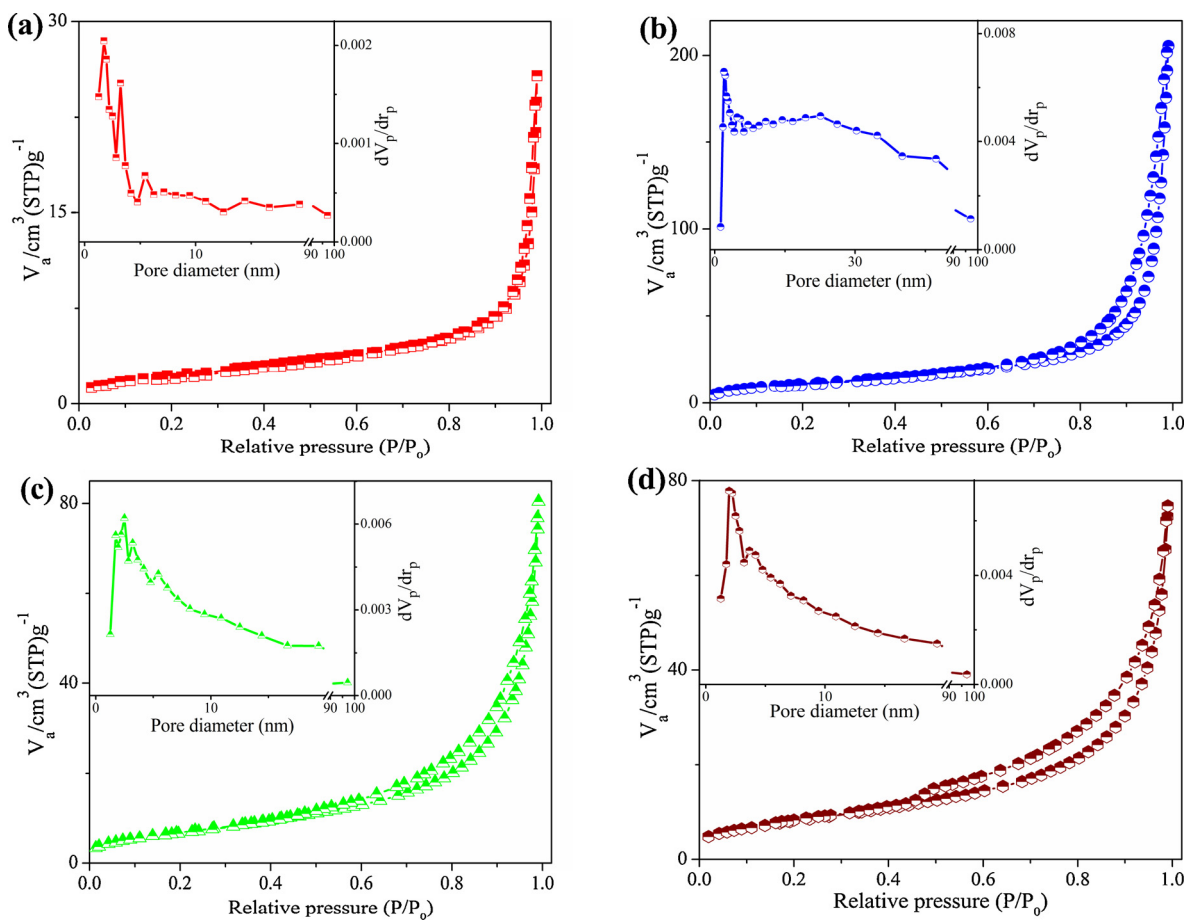**Fig. 4.** The SEM of (a)BOC, (b)BiO$_{2-x}$, (c) BiO$_{2-x}$-BiO$_{2-x}$(35 wt%) and (d) BOC-BiO$_{2-x}$(35 wt%)-GR.

Fig. 5. BET adsorption-desorption isotherms and pore size distribution of (a)BOC, (b)BiO$_{2-x}$, (c) BiO$_{2-x}$-BiO$_{2-x}$(35 wt%), and (d) BOC-BiO$_{2-x}$(35 wt%)-GR.

the flower-like hierarchical micro-sphere is built from numerous interlaced nanosheets in closed stacking. The BiO$_{2-x}$ is a shelf-like nanostructure made up of nanoplates that are almost perpendicular to each other (Fig. 4b). As shown in Fig. S4, GR is consisted of large and thin layers with ripples, which can certainly provide sufficient surface area to load the BOC or BiO$_{2-x}$ particles. As for BOC-BiO$_{2-x}$(35 wt%) composites, a few BiO$_{2-x}$ nanosheets were coated on the surface of BOC (Fig. 4c). As shown in Fig. 4d, both the micro-spheres BOC, BiO$_{2-x}$ nanosheets and GR sheets could be clearly observed in BOC-BiO$_{2-x}$(35 wt %)-GR. Notably, the BiO$_{2-x}$ nanosheets as well as micro-spheres BOC are well-decorated or intercalated on the surface of GR sheets to form a ternary heterojunction.

Fig. 5 shows the N$_2$ adsorption-desorption isotherms curves of BOC, BiO$_{2-x}$, BOC-BiO$_{2-x}$(35 wt%), and BOC-BiO$_{2-x}$(35 wt%)-GR. The Brunauer-Emmett-Teller (BET) specific surface area of BOC-BiO$_{2-x}$(35 wt%) (25.94 m^2/g) was estimated to be much higher than that of BiO$_{2-x}$ (8.51 m^2/g), and the BET surface area of BOC-BiO$_{2-x}$(35 wt%)-GR (29.65 m^2/g) was even higher. Therefore it is clear that GR indeed increased the surface area of the composite, which is expected to have favorable effect on the photocatalytic efficiency. It is also noted that the BET surface area of pure BOC was much larger than the composites, consistent with the different morphology of BOC and BiO$_{2-x}$ nanoparticles observed from the SEM inspections. According to the Barrett-Joyner-Halenda (BJH) pore size distribution curves (Inset of Fig. 5), the BOC and the composites show medium mesopores with peak pore diameters of about 2–4 nm, and large mesopores and macropores at a wide range of 10–100 nm. The medium mesopores can be ascribed to the pores formed among the aggregated BOC nanosheets and BiO$_{2-x}$ nanoparticles, and large mesopores and macropores are ascribed to the pores formed between the stacked BOC micro-spheres [16,21]. The

porous architectures may endow the BOC-based material with high surface area and better catalytic properties.

The TEM in Fig. 6a indicates that the BOC as well as BiO$_{2-x}$ are randomly decorated on or intercalated into GR sheets to form a ternary heterojunction. The HRTEM image (Fig. 6b) shows two different lattice fringes in the BOC-BiO$_{2-x}$(35 wt%)-GR. The corresponding interplanar spacings are about 0.29 and 0.318 nm, which correspond to the (013) plane of BOC and (111) plane of BiO$_{2-x}$ (Fig. 6c and d), respectively. As can be seen, BOC-BiO$_{2-x}$(35 wt%)-GR composites with close contact have been successfully fabricated. The crystal models of BOC-BiO$_{2-x}$ composites featured interfaces composed of BOC (013) and BiO$_{2-x}$(111) lattice planes is illustrated in Fig. 6e, the covalent bonding in the interfaces is generated by Bi atoms and the surface terminated O atoms.

3.2. Evaluation of photocatalytic activity

The as-synthesized BOC-BiO$_{2-x}$ sample with different BiO$_{2-x}$ mass ratios was investigated for the NO degradation at the indoor air level under simulated solar light irradiation to determine its capability for air purification. Fig. 7a displays the NO concentration changes (C$_t$/C$_0$) versus irradiation time in the presence of the different photocatalysts. Obviously, NO could not be removed via direct photolysis under simulated solar light irradiation without catalysts. BiO$_{2-x}$ alone displays poor activity (4.1% of NO removal ratio) due to the easy recombination of photo-induced charges. For pure BOC, the NO removal ratio was only 27.8% due to its large band gap and the fast recombination of e^--h^+ pairs [18–22]. Interestingly, the BOC-BiO$_{2-x}$ composites exhibited higher activity than either pure BOC or BiO$_{2-x}$. The removal ratio of NO with BOC-BiO$_{2-x}$(5 wt%), BOC-BiO$_{2-x}$(15 wt%), and BOC-BiO$_{2-x}$(25 wt %) are 46.4%, 49.4% and 50.5%, respectively (Fig. 7b). Particularly,
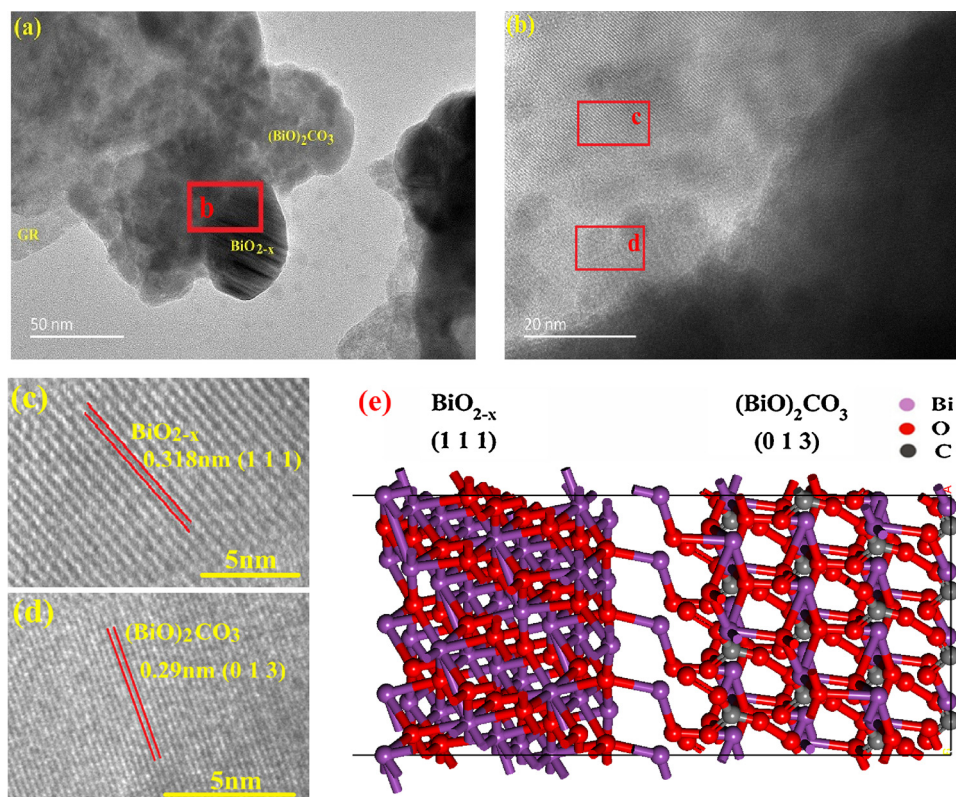
Fig. 6. TEM of BOC-BiO$_{2-x}$(35 wt%)-GR(a), (c, d) HRTEM image of BOC-BiO$_{2-x}$(35 wt%)-GR in the red frame of (b), and (e) optimized structure model of the BOC-BiO$_{2-x}$ interface. (For interpretation of the references to colour in this figure legend, the reader is referred to the web version of this article).

when the content of BiO$_{2-x}$ is of 35 wt%, BOC-BiO$_{2-x}$(35 wt%) demonstrated the highest photocatalytic activity with a NO removal ratio of 53.6%, which surpassed that of BOC by more than 25.8% (Fig. 7b). This high photocatalytic performance may be benefited from the enhanced light absorption, effective charge transfer and intimate contact between BOC and BiO$_{2-x}$. A further increase in the amount for BiO$_{2-x}$(45 wt%) results in a decrease of activity, but it is still higher than those of pure BOC and BiO$_{2-x}$. There are two reasons which may explain this reduction of activity: 1) A high content of BiO$_{2-x}$ could block the slit-shaped pores of BOC for the adsorption of NO molecules. 2) Overmuch BiO$_{2-x}$ has a relative poor photocatalytic activity of NO removal under the same photo-irradiation conditions. Therefore, loading appropriate amounts of BiO$_{2-x}$ can optimize the photocatalytic activity of the BOC.

Fig. 7c shows that the photocatalytic activity of the binary composite can be further improved by the addition of GR. For comparison, NO degradation over BiO$_{2-x}$-GR and BOC-GR were also carried out under identical conditions. Interestingly, all three composites with GR, i.e., BiO$_{2-x}$-GR, BOC-GR and BOC-BiO$_{2-x}$(35 wt%)-GR, showed significant improvement in the photocatalytic efficient as compared to the corresponding materials without GR. For example, after 30 min simulated solar light illumination nearly 38.4% of NO was removed by BOC-GR while only 27.8% of NO was removed by pure BOC. Overall the BOC-BiO$_{2-x}$(35 wt%)-GR nanocomposites exhibited the largest degradation ability (60.7%) among all the photocatalysts, which can be possibly attributed to both efficient electron transfer through the interfaces and the enlarged specific surface area provided by GR.

The influence of the initial concentration of NO on the photocatalytic activity of the BOC-BiO$_{2-x}$(35 wt%)-GR composite was also investigated and are shown in Fig. S5a and b. It was found that in the NO concentration range between 150 ppb–500 ppb, the removal efficiency of NO reaches the maximum at 430 ppb.

The stability and recyclability of BOC-BiO$_{2-x}$(35 wt%)-GR nanocomposites were evaluated through multiple photocatalytic experiments over used BOC-BiO$_{2-x}$(35 wt%)-GR photocatalyst (Fig. 7d). The NO removal ratio were 60.7%, 60.1%, 58.1%, 56.8%, and 54.9% from the first to the fifth cycles, respectively, showing only slight decrease in efficiency. In addition, Fig. 7b implies that BOC-BiO$_{2-x}$(35 wt%)-GR could maintain about 54.9% of NO removal for at least 90 min irradiation, which can be considered as a suitable photocatalyst for practical applications. Additionally, the used catalyst after reaction was examined by XRD, XPS and SEM. As shown in Fig. S6a–d, the diffraction peaks, surface chemical composition, and morphology remained almost the same, suggesting the stability of the as-prepared materials during the photocatalytic reactions.

3.3. Photocatalytic mechanism analyses

Fig. 8a shows the transient photocurrent responses which can be used to analyze the efficiency of charge generation and separation under simulated solar light irradiation. The photocurrent of the BOC and BiO$_{2-x}$ anode were about 0.8 and 1 µm/cm^2, whereas the photocurrent value of BOC-BiO$_{2-x}$(35 wt%) electrode reached as high as 2 µA/cm^2, nearly 2.5 times of pure BOC. The much higher photocurrent intensity in BOC-BiO$_{2-x}$(35 wt%) can be ascribed to the introduction of BiO$_{2-x}$, and it is obvious that electrons and holes were separated more effectively in BOC-BiO$_{2-x}$(35 wt%). Furthermore, BOC-BiO$_{2-x}$(35 wt%)-GR showed additional photocurrent intensity enhancement. The BOC-BiO$_{2-x}$(35 wt%)-GR photoelectrode exhibits the highest photocurrent density of 2.4 µA/cm^2, which is about 1.2 times than that of BOC-BiO$_{2-x}$(35 wt%) photoelectrode. The above observation evidenced that GR can indeed act as an electron transport bridge, which accelerates the electron transfer from BiO$_{2-x}$ to BOC. Meanwhile, PL is employed to further confirm the positive effect of the GR on the dynamics of interfacial charge transfer under same conditions. As presented in Fig. S7, the BOC-BiO$_{2-x}$(35 wt%)-GR displays lower PL intensity than that BOC-BiO$_{2-x}$(35 wt%). This result indicated that the introduction of
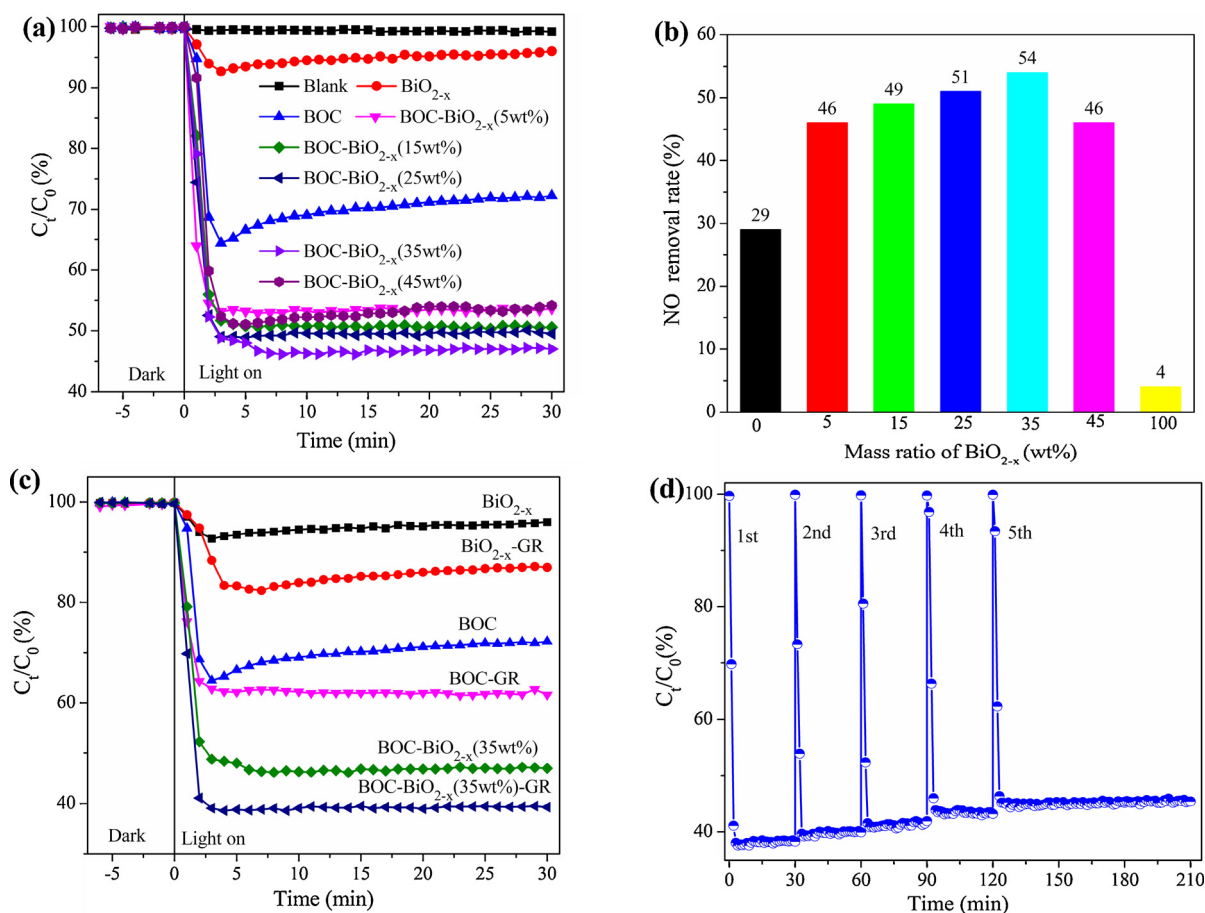
Fig. 7. (a, b) Comparison of photocatalytic activities and removal rate towards NO by BOC-BiO$_{2-x}$, (c) photocatalytic activity evaluation of different photocatalysts, and (d) cycle photocatalytic performance of BOC-BiO$_{2-x}$(35 wt%)-GR under simulated solar light irradiation.

appropriate GR into BOC-BiO$_{2-x}$(35 wt%) is an effective way to promote the photogenerated electron-hole pairs separation and the interfacial charge transfer, which is consistent with the results of photocurrent.

The SPV as a well-established non-contact method, could effectively reflect the information about the process of photoinduced charge separation and transfer in the surface and interface under monochromic excitation. Generally, a stronger SPV response signal implies a higher separation efficiency of photo-generated charges under the illuminated condition [8]. Fig. 8b shows the SPV spectra of all the samples. Pure

BOC (the inset of Fig. 8b) and BiO$_{2-x}$ present a clear positive SPV signal after being excited by light with wavelength ranging from 300 to 600 nm, which is a typical characteristic of n-type semiconductor in SPV [15]. The BOC-BiO$_{2-x}$(35 wt%) composites exhibited higher SPV intensity than pure BOC and BiO$_{2-x}$, indicating that there should be strong interaction between BOC and BiO$_{2-x}$ in the hydrothermal process, which plays an important role in the transfer of photogenerated carriers. The BOC-BiO$_{2-x}$(35 wt%)-GR sample shows the highest SPV intensity, in turns most efficient charge separation efficiency, which is
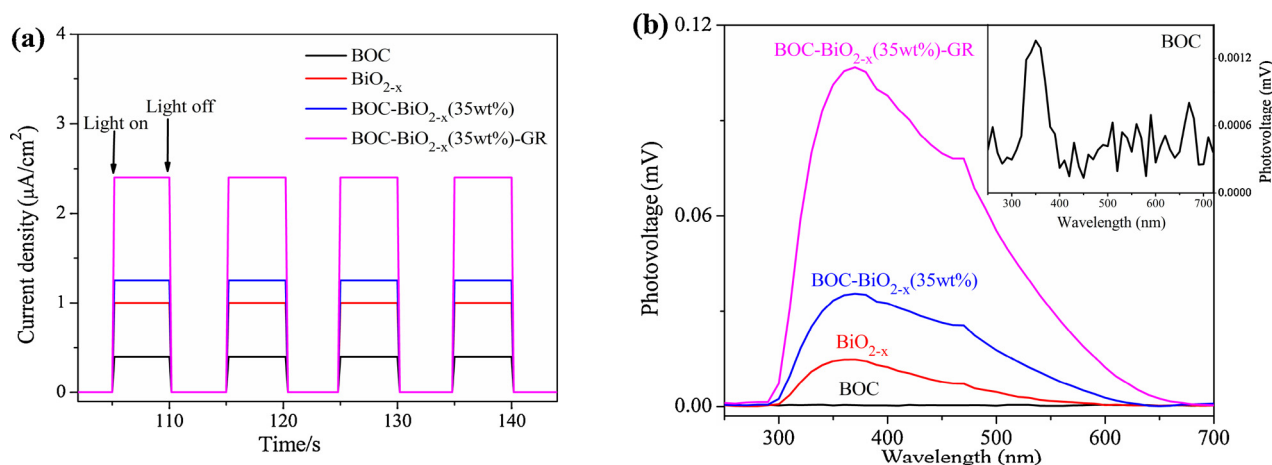

Fig. 8. (a) Photocurrent and (b) surface photovoltage (SPV) spectra of BOC, BiO$_{2-x}$, BiO$_{2-x}$-BiO$_{2-x}$(35 wt%) and BOC-BiO$_{2-x}$(35 wt%)-GR (the inset is the SPV spectra of BOC).
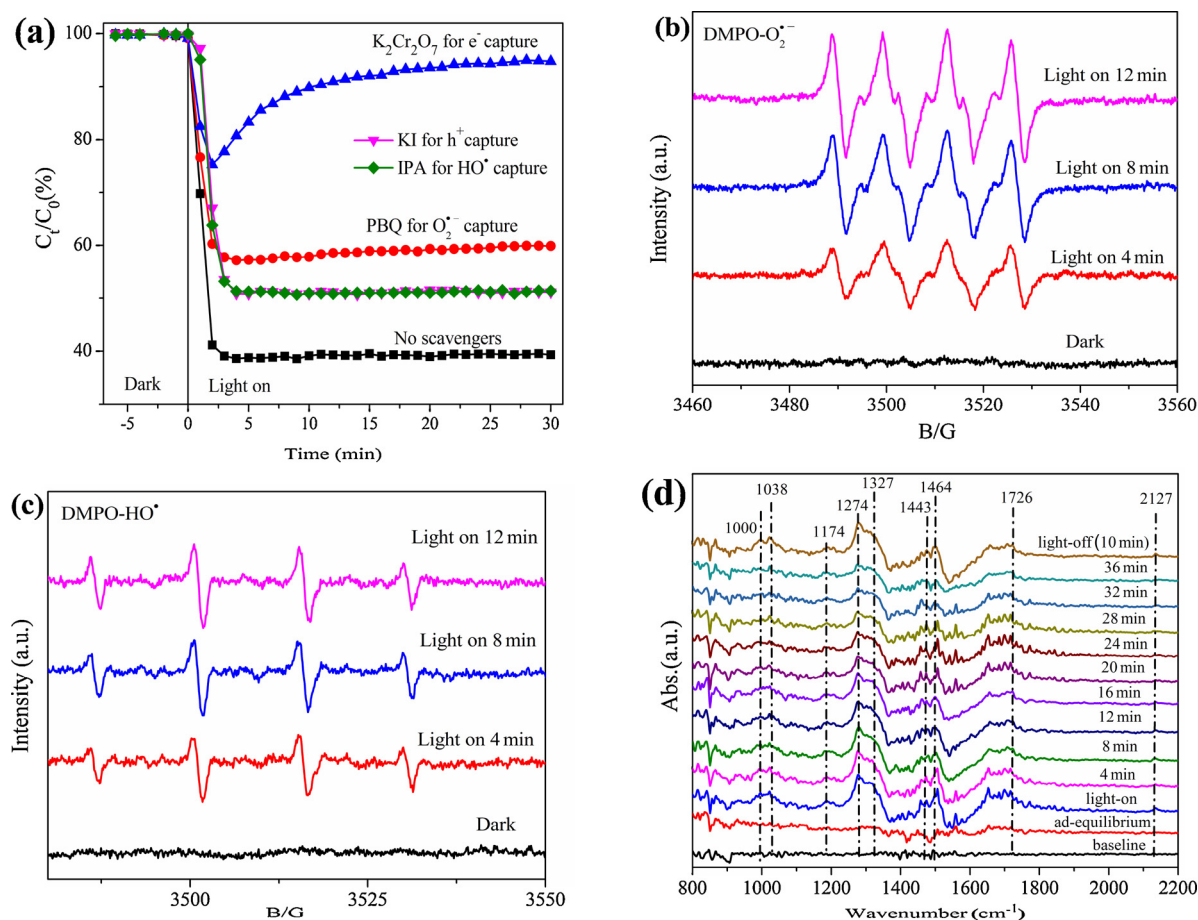
Fig. 9. (a) Active specices trapping experiments, ESR signals of the (b) DMPO-$O_2^{\cdot-}$ and (c) DMPO-HO$^\cdot$ for BOC-BiO$_{2-x}$(35 wt%)-GR under simulated solar light irradiation, and (d) in situ FT-IR spectra of photocatalytic NO oxidation process over BOC-BiO$_{2-x}$(35 wt%)-GR.

also consistent with the results of photocatalytic experiment. The enhanced separation efficiency of electron-hole pairs can be attributed to GR as a mediator can promote the electrons transfer from BOC to BiO$_{2-x}$ through a Z-scheme mechanism. The results are consistent with the analysis of the photocurrent and PL characterization.

Before proposing the reaction mechanism of photocatalytic NO oxidation, the scavenger experiments and ESR were carried out to determine the type of active species and their contributions. In these trapping experiments, KI, $K_2Cr_2O_7$, isopropyl alcohol (IPA), and p-benzoquinone (PBQ) were selected to trap the photogenerated h^+, e^-, hydroxide radical (HO$^\cdot$), and superoxide anion radical ($O_2^{\cdot-}$) species [36,37], respectively. It's worth noting that the addition of $K_2Cr_2O_7$ significantly decreased the NO removal activity, whereas the inhibition effect imposed by KI, IPA and PBQ are far less than $K_2Cr_2O_7$ (Fig. 9a). These results implied that the photogenerated e^- played the most important role in NO removal. Since the photogenerated e^- can activate O_2 to produce active $O_2^{\cdot-}$ and HO$^\cdot$ from the oxidation H_2O with h^+, it is essential to investigate the role of these active oxygen species in the NO removal process.

ESR spectroscopy with DMPO spin-trapping adducts was performed to allow the detection of $O_2^{\cdot-}$ radicals (DMPO-$O_2^{\cdot-}$) in methanol and HO$^\cdot$ radicals (DMPO-HO$^\cdot$) in aqueous state. As shown in Fig. 9b, there was no signal when the system in the dark, while four apparent signals of DMPO-$O_2^{\cdot-}$ could be clearly observed once BOC-BiO$_{2-x}$(35 wt%)-GR were exposed to simulated solar light irradiation. In addition, the DMPO-$O_2^{\cdot-}$ signal intensities increased with the irradiation time. In Fig. 11c, the DMPO-HO$^\cdot$ signal could be not detected under dark conditions. Under simulated solar light illumination, four characteristic peaks with intensity ratio of 1:2:2:1 for DMPO-HO$^\cdot$ adducts were

observed. This indicates that HO$^\cdot$ radicals are generated on the sample after irradiation. These results imply that both the $O_2^{\cdot-}$ and HO$^\cdot$ radicals are responsible for the photocatalytic oxidation of NO in air. This is in accord with the results of trapping experiments.

Fig. 9d shows the in situ FT-IR spectra of the NO adsorption in the dark and photocatalytic reaction processes on the surface of BOC-BiO$_{2-x}$(35 wt%)-GR under simulated solar light irradiation. Table S1 summarizes the assignment of the corresponding main adsorption peaks. In dark, the absorption peak of bidentate NO_3^- (1038 cm^{-1}) can be observed after adsorption equilibrium [36]. This could be attributed to the oxygen vacancies in BiO$_{2-x}$ that reacted with the adsorbed O_2 to produce $\cdot O_2^-$ [23,25], which consequently oxidized NO to bidentate NO_3^-. After turning the light on, a lot of enhanced absorption peaks such as bridging NO_3^- (1000 cm^{-1}), chelate NO_2^- (1174 cm^{-1}), bidentate NO_3^- (1038 cm^{-1}), N_2O_4 (1274 and 1726 cm^{-1}), NO_2^- (1327 cm^{-1}), NO_2 (1443 and 1464 cm^{-1}), and NO^+ (2127 cm^{-1}) can be detected [36,38–40], which further confirmed that NO was oxidized by the active species generated under simulated solar light irradiation, in good consistency with the transient decrease of the NO concentration after exposing to the solar light for the first 2 min in Fig. 7a. As evidenced by the scavenger experiments and ESR, the h^+, $O_2^{\cdot-}$ and HO$^\cdot$ (Eq. (1)–(3) are main reactive species for the photocatalytic oxidation of NO. The intermediate NO_2 comes from the oxidization of NO with the HO$^\cdot$ and O_2 (Eqs. (4) and (5)), whereas the NO_2 may be further converted to N_2O_4 (Eq. (5) or absorbed by H_2O or alkali liquor to form NO_3^- and NO2- (Eq. (6), which are good nitrogen fertilizer [41].The production of NO^+ intermediates should be ascribed to the partial oxidation of NO with the HO$^\cdot$ and h^+ (Eqs. (7) and (8)). The NO^+ intermediates undergo further reactions following Eqs. (9) and (10) and
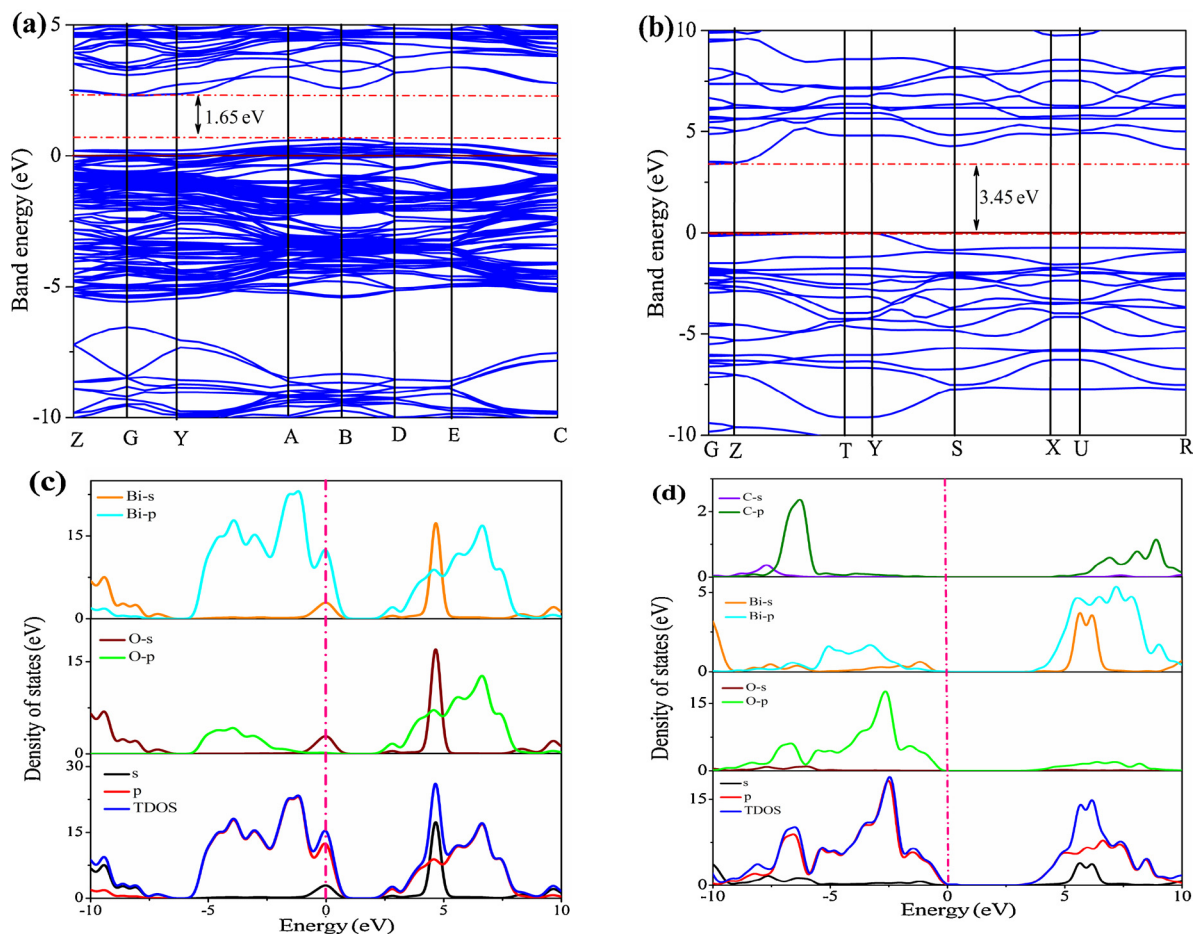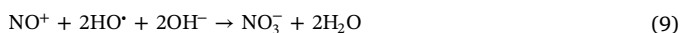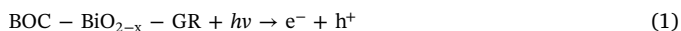
Fig. 10. (a, b) Band structure and (c, d) partial and total density of states (PDOS and TDOS) for BiO_{2-x} and BOC.

generate the final products nitrite and nitrate. Therefore, the formation of NO^+ could promote the NO photocatalytic oxidization. In addition, as very strong oxidizing agents, the $O_2^{\cdot-}$ and h^+ radicals can oxidize NO into the final NO_3^- (Eqs. (11) and (12)). Since the final products of NO_3^- and NO_2^- are still presented on the surface of the photocatalyst after the reaction (light off 10 min). This is the main reason for the gradual decrease in photocatalyst activity during the recycling experiment. However, the detail mechanism and intermediate products in the photocatalytic NO oxidation process need further study in the future. Based on the above results and analyses, the possible photocatalytic reaction processes were listed as follows (Eqs. (1)–(12)):

$$BOC - BiO_{2-x} - GR + h\nu \rightarrow e^- + h^+ \tag{1}$$

$$e^- + O_2 \rightarrow O_2^{\cdot-} \tag{2}$$

$$h^+ + OH^- \rightarrow HO^\cdot \tag{3}$$

$$NO + 2HO^\cdot \rightarrow NO_2 + H_2O \tag{4}$$

$$2NO + 2O_2 \rightarrow 2NO_2 \Leftrightarrow N_2O_4 \tag{5}$$

$$2NO_2 + H_2O \rightarrow HNO_3 + HNO_2 \tag{6}$$

$$NO + HO^\cdot \rightarrow NO^+ + OH^- \tag{7}$$

$$h^+ + NO \rightarrow NO^+ \tag{8}$$

$$NO^+ + 2HO^\cdot + 2OH^- \rightarrow NO_3^- + 2H_2O \tag{9}$$

$$NO^+ + 2OH^- \rightarrow NO_2^- + H_2O \tag{10}$$

$$NO + O_2^{\cdot-} \rightarrow NO_3^- \tag{11}$$

$$h^+ + NO + H_2O \rightarrow NO_3^- + 2H^+ \tag{12}$$

In this section, considering on the experimental observations stated above, we attempt to discuss the photocatalytic mechanism of the ternary composite together with related theoretical calculations. The most important point is the charge transfer between these three materials, which can only be discussed unambiguously based on the bandgap energies and energy band positions of BOC and BiO_{2-x}.

Mott-Schottky plot was first measured to locate the conduction band (CB) edges of BOC and BiO_{2-x}. As shown in Fig. S9, the positive slope of the C^{-2}-E plot suggested that both BOC and BiO_{2-x} are n-type semiconductors, which is consistent with the results of SPV. The flat band potential (E_{fb}) of BOC and BiO_{2-x} are located at -0 and -0.7 V vs. SCE, which corresponds to 0.24 and -0.46 V vs. NHE, respectively. Since the E_{fb} of the n-type semiconductor may be considered approximately as the conduction band (CB) edge [34]. The E_{CB} of BOC and BiO_{2-x} are estimated to be 0.24 and -0.46 V vs. NHE, respectively. The energy positions of the valence band edge (E_{VB}) and conduction band edge (E_{CB}) of BOC and BiO_{2-x} are then calculated according to the following equations [42]:

$$E_{CB} = E_{VB} - E_g \tag{13}$$

where E_g is the band gap of the semiconductor. Here we use the bandgap energy values obtained from the UV–vis absorption spectra, which is 3.45 eV (BOC) and 1.68 eV (BiO_{2-x}). Accordingly, the positives of E_{VB} of BOC and BiO_{2-x} are estimated to be 3.69 and 1.22 V vs. NHE, respectively.

The CB energy difference between BOC and BiO_{2-x} is 0.70 eV, and the VB energy difference BOC and BiO_{2-x} is 2.47 eV. In this case, the electrons might migrate between the energy levels in Z-scheme or type-II situations. Therefore further information is necessary to determine
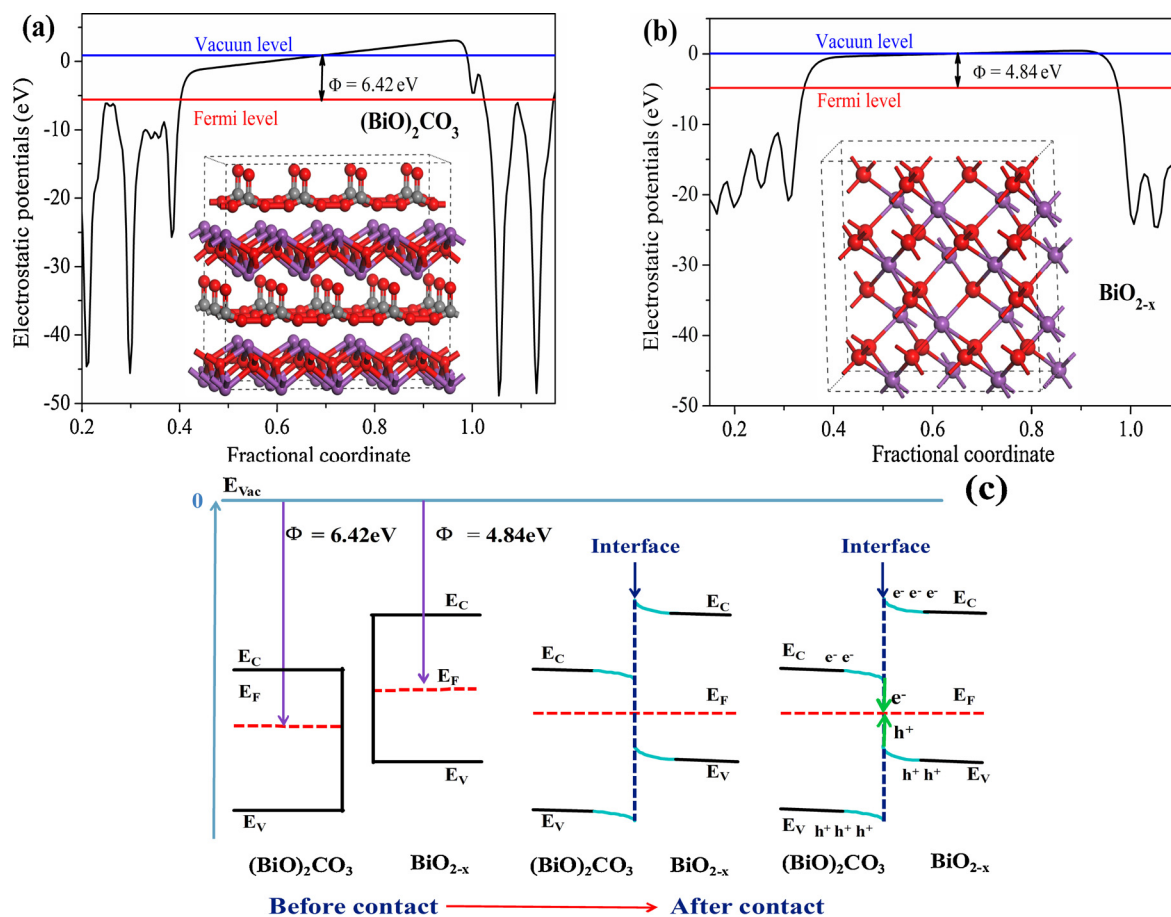
Fig. 11. Calculated electrostatic potentials for BOC and BiO$_{2-x}$, respectively. The gray, red, and purple spheres are C, O, and Bi atoms. (c) The interface band bending diagram and interfacial electron transfer between BOC and BiO$_{2-x}$. (For interpretation of the references to colour in this figure legend, the reader is referred to the web version of this article).
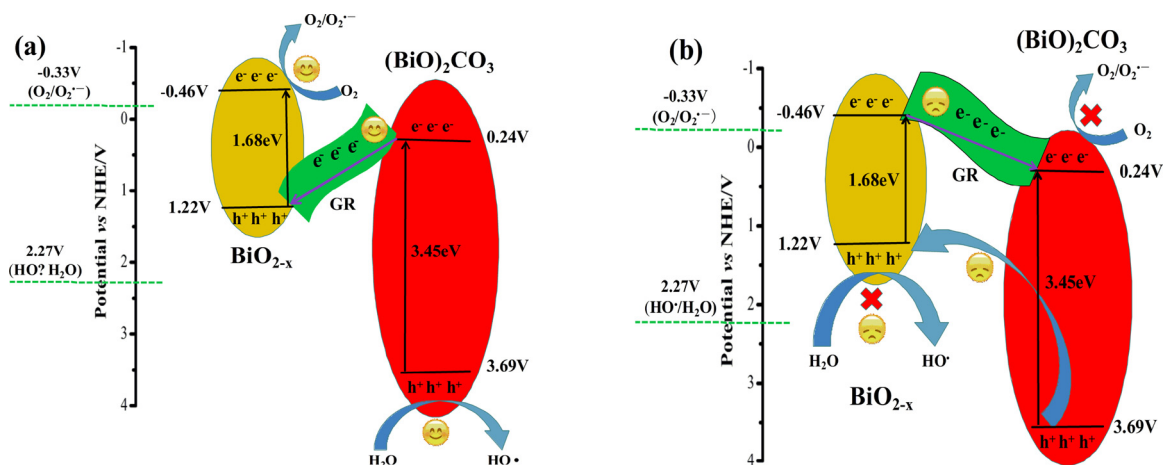

Fig. 12. Two models of charge separation proposed for BOC-BiO$_{2-x}$(35 wt%)-GR under simulated solar light irradiation: (a) Z-scheme electron transfer and (b) Conventional donor acceptor charge transfer.

the charge transfer behavior between BOC and BiO$_{2-x}$.

Band structures and partial/total density of states (PDOS/TDOS) for BiO$_{2-x}$ and BOC are simulated based on DFT method and illustrated in Fig. 10. The calculated band gap value can be measured as about 1.65 eV for BiO$_{2-x}$ and 3.40 eV for BOC (Fig. 10a and b). The calculated band gap value of BiO$_{2-x}$ and BOC are narrower than experimental results by DRS spectra (1.68 eV for BiO$_{2-x}$ and 3.45 eV for BOC), which may be resulted from the well-known limitation of generalized gradient approximation (GGA). From the DOS shown in Fig. 10c, the BiO$_{2-x}$ show

a half-metallic characteristic, mostly originated from the O2p and Bi4p states. The valence band (VB) of BiO$_{2-x}$ is composed of Bi4p and O2p, while the conduction band (CB) edge is basically composed of Bi4p, Bi4s, O2p, and O2s orbits. The VB electrons in BiO$_{2-x}$ are easily excited, due to low hybridization between O atoms and adjacent Bi atoms in the VB, half-metallic characteristics, and small band gap. Nevertheless, due to the large hybrid electron density of Bi atoms with O atoms nearby in the CB, the CB electrons mostly transfer inside the BiO$_{2-x}$ to cause high recombination of photogenerated electrical carriers. For BOC

(Fig. 10d), the CB edge is basically composed of Bi6p, Bi6s, O2p, and C2p orbits, while the VB edge is mainly originated from O2p, Bi6p, and C2p orbits. The VB electrons of BOC are difficult to be excited, due to the wide band gap of BOC and the O atoms, Bi atoms, and adjacent C atoms are well hybridized in VB. It is owing to the fact that large hybrid electron density of O atoms with neighboring C and Bi atoms enhances electrostatic attraction between the nucleus and electrons. On the other hand, the CB electrons can be easily excited and migrate to the surface of BOC due to the low hybridization. Therefore, in the BOC-BiO$_{2-x}$ heterojunction the CB electrons in BOC and holes left in the VB of BiO$_{2-x}$ are more active, which can have a determinant effect on the charge transfer dynamic in the BOC-BiO$_{2-x}$-GR composite. However, the charge transfer between BOC and BiO$_{2-x}$ depends on the interfacial band bending, which is further determined by Fermi levels and the energy band of BOC and BiO$_{2-x}$.

Furthermore, the calculation on Fermi levels indicated that the band bending in BOC and BiO$_{2-x}$ at the interface of the heterojunction favors the re-combination of CB electrons on BOC and the VB holes in BiO$_{2-x}$. Fig. 11a and b shows the calculated electrostatic potentials of BOC(013) and BiO$_{2-x}$(111), the work functions of BOC(013) and BiO$_{2-x}$(111) were calculated to be 6.42 and 4.84 eV, respectively, which means the Fermi level of BiO$_{2-x}$ is higher than that of BOC. In this case, when BOC contacts with BiO$_{2-x}$, electrons of BiO$_{2-x}$ should transfer to BOC till the Fermi energies of these two constituents are aligned (Fig. 11c). As a result, the energy band edges in BiO$_{2-x}$ with high Fermi level are bended upward continuously toward the interface, and those in BOC with low Fermi level are bended downward towards the interface (Fig. 11c) [43,44]. Therefore, the CB electrons in BOC are allowed to flow out freely while the holes are confined in the VB. On the other hand, since the energy band of BiO$_{2-x}$ is bended upward near the interface, holes in VB can easily migrate to the interface. Consequently, the photo-induced electrons of BOC and holes of BiO$_{2-x}$ will transfer to the interface but can not flow into the energy bands of the other semiconductor, so they can only recombine with each other at the interface (Fig. 11c). The CB electrons of BiO$_{2-x}$ and VB holes of BOC are remained in their original energy bands to participate in photocatalysis of NO. Through the above theoretical calculation results, it is clear that the BOC-BiO$_{2-x}$(35 wt %)-GR composite can be considered as a Z-scheme photocatalyst.

Finally, we propose the separation processes of photoexcited $e^- $-$h^+$ and the photocatalytic mechanism of NO degradation using BOC-BiO$_{2-x}$-GR. According to the above discussion and periodic DFT simulations, a possible Z-scheme charge transfer is illustrated in Fig. 12a. In this case, the photogenerated e^- in the CB of BOC would be transferred and recombined with h^+ in the VB of BiO$_{2-x}$. The photogenerated e^- in BiO$_{2-x}$ remained in the CB of BiO$_{2-x}$, and h^+ in BOC remained in the VB of BOC. The migration of charge carrier can result in the e^- accumulating in the CB of BiO$_{2-x}$, and the h^+ retained in the VB of BOC. The CB potential of BiO$_{2-x}$(-0.46 V vs. NHE) is more negative than the O$_2$/O$_2^{·-}$ reduction potential (-0.33 V vs. NHE) [45,46], and the VB potential of BOC (3.69 V vs. NHE) is more positive than the standard redox potential of H$_2$O/HO$^·$ (2.27 V vs. NHE) [47]. This means that the e^- in CB of BiO$_{2-x}$ could be trapped by O$_2$ to form the reactive O$_2^{·-}$, whereas the h^+ left in the VB of BOC have enough energy to reduce H$_2$O to produce HO$^·$ radicals, which is consistent with the ESR results. Both O$_2^{·-}$ and HO$^·$ radicals subsequently participate in the removal of NO.

The high efficient photocatalytic performance observed experimentally as presented in section 3.2 confirmed that the Z-scheme charge transfer is indeed dominant in the BOC-BiO$_{2-x}$-GR photocatalyst. If the charge transfer follows the mechanism of the type-II semiconductor heterojunction (Fig. 12b), the photo-generated e^- should migrate from the CB of BiO$_{2-x}$(-0.46 V vs. NHE) to BOC (0.24 V vs. NHE), and the photogenerated h^+ in the VB of BOC(3.69 V vs. NHE) would migrate to the VB of BiO$_{2-x}$ (1.22 V vs. NHE). In this case, neither e^- nor h^+ can participate in the reduction or oxidation process because of the energy band level. However, the trapping experiment and ESR results indicated that O$_2^{·-}$ and HO$^·$ are the predominant active species

for the BOC-BiO$_{2-x}$-GR system. Therefore, it is reasonable to conclude that the photogenerated $e^- $-$h^+$ in BOC-BiO$_{2-x}$-GR hybrids did not transfer via the conventional heterojunction process in Fig. 12b.

Overall, the combination of BOC, BiO$_{2-x}$, and GR into one composite material showed synergy effect in enhancing the simulated solar light photocatalytic degradation of NO. BiO$_{2-x}$ provided not only a high absorption of simulated solar light but also a transfer and separation path of electrons from BOC. GR further enhanced the electron transfer by acting as a high conducting interface material between BiO$_{2-x}$ and BOC, and at the same time increased the surface area due to its 2D layered morphology. Therefore, the high photocatalytic efficiency observed in the BOC-BiO$_{2-x}$-GR photocatalysts can be attributed to the above two factors.

4. Conclusions

In summary, noble metal free, simulated solar light responsive, highly reactive and stable BOC-BiO$_{2-x}$-GR photocatalyst was successfully constructed. The NO removal efficiency as high as 61% was observed, and no obvious deactivated of the photocatalyst was caused by the photocatalytic process. Based on the experimental and computation results demonstrate that Z-scheme charge transfer was proposed to explain the observed high photocatalytic efficiency. The introduction of GR is important because its high conductivity can promote the migration of electrons and its 2D morphology can provide large surface area. It is believed that the design rules used in the present work can be extended to construct other BiO$_{2-x}$-based Z-scheme heterostructure photocatalytic systems for simulated solar light removal of air pollution.

Acknowledgments

Appendix A. Supplementary data

Supplementary material related to this article can be found, in the online version, at doi:https://doi.org/10.1016/j.apcatb.2018.09.005.

References

[1] Y. Huang, Y. Gao, Q. Zhang, Y. Zhang, J. Cao, W. Ho, S.C. Lee, Biocompatible FeOOH-carbon quantum dots nanocomposites for gaseous NO$_x$ removal under visible light: improved charge separation and high selectivity, J. Hazard. Mater. 354 (2018) 54–62.

[2] X. Ding, W. Ho, J. Shang, L. Zhang, Self doping promoted photocatalytic removal of NO under visible light with Bi$_2$MoO$_6$: indispensable role of superoxide ions, Appl. Catal. B 182 (2016) 316–325.

[3] D.S. Bhatkhande, V.G. Pangarkar, A.A. Beenackers, Photocatalytic degradation for environmental applications-a review, J. Chem. Technol. Biotechnol. 77 (2002) 102–116.

[4] J.M. Barnes, W.A. Apel, K.B. Barrett, Removal of nitrogen oxides from gas streams using biofiltration, J. Hazard. Mater. 41 (1995) 315–326.

[5] H. Xu, Y. Wang, Y. Cao, Z. Fang, T. Lin, M. Gong, Y. Chen, Catalytic performance of acidic zirconium-based composite oxides monolithic catalyst on selective catalytic reduction of NO$_x$ with NH$_3$, Chem. Eng. J. 240 (2014) 62–73.

[6] A. Boubnov, H.W. Carvalho, D.E. Doronkin, T. Günter, E. Gallo, A.J. Atkins, J.D. Grunwaldt, Selective catalytic reduction of NO over Fe-ZSM-5: mechanistic insights by operando HERFD-XANES and valence-to-core X-ray emission spectroscopy, J. Am. Chem. Soc. 136 (2014) 13006–13015.

[7] Z. Ai, W. Ho, S. Lee, L. Zhang, Efficient photocatalytic removal of NO in indoor air with hierarchical bismuth oxybromide nanoplate microspheres under visible light, Environ. Sci. Technol. 43 (2009) 4143–4150.

[8] Q. Zhang, Y. Huang, S. Peng, Y. Zhang, Z. Shen, J.J. Cao, D.Y. Pui, Perovskite LaFeO$_3$-SrTiO$_3$ composite for synergistically enhanced NO removal under visible

light excitation, Appl. Catal. B 204 (2017) 346–357.

[9] I. Papailias, N. Todorova, T. Giannakopoulou, N. Ioannidis, N. Boukos, C.P. Athanasekou, D. Dimotikal, C. Trapalis, Chemical vs thermal exfoliation of g-C₃N₄ for NOₓ removal under visible light irradiation, Appl. Catal. B 239 (2018) 16–26.

[10] A. Trapalis, N. Todorova, T. Giannakopoulou, N. Boukos, T. Speliotis, D. Dimotikali, J. Yu, TiO₂/graphene composite photocatalysts for NOₓ removal: a comparison of surfactant-stabilized graphene and reduced graphene oxide, Appl. Catal. B 180 (2016) 637–647.

[11] Z. Wang, S. Yan, Y. Sun, T. Xiong, F. Dong, W. Zhang, Bi metal sphere/graphene oxide nanohybrids with enhanced direct plasmonic photocatalysis, Appl. Catal. B 214 (2017) 148–157.

[12] F. Dong, Q. Li, Y. Sun, W.K. Ho, Noble metal-like behavior of plasmonic Bi particles as a cocatalyst deposited on (BiO)₂CO₃ microspheres for efficient visible light photocatalysis, ACS Catal. 4 (2014) 4341–4350.

[13] A. Nikokavoura, C. Trapalis, Graphene and g-C₃N₄ based photocatalysts for NOₓ removal: a review, Appl. Surf. Sci. 430 (2018) 18–52.

[14] M. Ou, Q. Zhong, S. Zhang, H. Nie, Z. Lv, W. Cai, Graphene-decorated 3D BiVO₄ superstructure: highly reactive (040) facets formation and enhanced visible-light-induced photocatalytic oxidation of NO in gas phase, Appl. Catal. B 193 (2016) 160–169.

[15] M. Chen, J. Yao, Y. Huang, H. Gong, W. Chu, Enhanced photocatalytic degradation of ciprofloxacin over Bi₂O₃/(BiO)₂CO₃ heterojunctions: efficiency, kinetics, pathways, mechanisms and toxicity evaluation, Chem. Eng. J. 334 (2018) 453–461.

[16] T. Xiong, H. Huang, Y. Sun, F. Dong, In situ synthesis of a C-doped (BiO)₂CO₃ hierarchical self-assembly effectively promoting visible light photocatalysis, J. Mater. Chem. A 3 (2015) 6118–6127.

[17] T. Xiong, X.A. Dong, H. Huang, W. Cen, Y. Zhang, F. Dong, Single precursor mediated-synthesis of Bi semimetal deposited N-doped (BiO)₂CO₃ superstructures for highly promoted photocatalysis, ACS Sustain. Chem. Eng. 4 (2016) 2969–2979.

[18] Z. Wang, Y. Huang, W. Ho, J. Cao, Z. Shen, S.C. Lee, Fabrication of Bi₂O₂CO₃/g-C₃N₄ heterojunctions for efficiently photocatalytic NO in air removal: in-situ self-sacrificial synthesis, characterizations and mechanistic study, Appl. Catal. B 199 (2016) 123–133.

[19] Y. Huang, D. Zhu, Q. Zhang, Y. Zhang, J.-j. Cao, Z. Shen, W. Ho, S.C. Lee, Synthesis of a Bi₂O₂CO₃/ZnFe₂O₄ heterojunction with enhanced photocatalytic activity for visible light irradiation-induced NO removal, Appl. Catal. B 234 (2018) 70–78.

[20] T. Xiong, M. Wen, F. Dong, J. Yu, L. Han, B. Lei, Z. Zang, Three dimensional Z-scheme (BiO)₂CO₃/MoS₂ with enhanced visible light photocatalytic NO removal, Appl. Catal. B 199 (2016) 87–95.

[21] J. Hu, D. Chen, N. Li, Q. Xu, H. Li, J. He, J. Lu, In situ fabrication of (BiO)₂CO₃/MoS₂ on carbon nanofibers for efficient photocatalytic removal of NO under visible-light irradiation, Appl. Catal. B 217 (2017) 224–231.

[22] L. Liang, J. Cao, H. Lin, M. Zhang, X. Guo, S. Chen, A novel double visible light active Z-scheme AgI/Ag/I-(BiO)₂CO₃ composite: automatic formation of Ag bridge in the photocatalytic process, Mater. Res. Bull. 94 (2017) 291–297.

[23] J. Li, X. Wu, W. Pan, G. Zhang, H. Chen, Vacancy-rich monolayer BiO₂₋ₓ as a highly efficient UV, visible, and near-infrared responsive photocatalyst, Angew. Chem. Int. Ed. 57 (2018) 491–495.

[24] L.N. Li, T.H. Chen, Z.S. Liu, P.Z. Feng, Novel BiO₂₋ₓ photocatalyst: typical hierarchical architecture and commendable activity, Mater. Lett. 212 (2018) 267–270.

[25] H. Sun, H.Y. Yip, Z. Jiang, L. Ye, I. Lo, P.K. Wong, Facile synthesis of oxygen defective yolk-shell BiO₂₋ₓ for visible-light-driven photocatalytic inactivation of Escherichia coli, J. Mater. Chem. A 6 (2018) 4997–5005.

[26] L. Jin, G. Zhu, M. Hojamberdiev, X. Luo, C. Tan, J. Peng, X. Wei, J. Li, P. Liu, A plasmonic Ag-AgBr/(BiO)₂CO₃ composite photocatalyst with enhanced visible-light photocatalytic activity, Ind. Eng. Chem. Res. 53 (2014) 2127–2134.

[27] Z. Ni, Y. Sun, Y. Zhang, F. Dong, Fabrication, modification and application of (BiO)₂CO₃-based photocatalysts: a review, Appl. Surf. Sci. 365 (2016) 314–335.

[28] X. Li, X. Yan, X. Lu, S. Zuo, Z. Li, C. Yao, C. Ni, Photo-assisted selective catalytic reduction of NO by Z-scheme natural clay based photocatalyst: insight into the effect of graphene coupling, J. Catal. 357 (2018) 59–68.

[29] X. Zeng, Z. Wang, N. Meng, D.T. Mccarthy, A. Deletic, J.H. Pan, Highly dispersed TiO₂, nanocrystals and carbon dots on reduced graphene oxide: ternary

[30] W. Zhang, F. Dong, W. Zhang, Capture of atmospheric CO₂, into (BiO)₂CO₃/graphene or graphene oxide nanocomposites with enhanced photocatalytic performance, Appl. Surf. Sci. 358 (2015) 75–83.

[31] M. Chen, Y. Huang, J. Yao, J. Cao, liu Y, Visible-light-driven N-(BiO)₂CO₃/Graphene oxide composites with improved photocatalytic activity and selectivity for NOₓ removal, Appl. Surf. Sci. 430 (2018) 137–144.

[32] Z. Tong, Y. Dong, J. Shi, Y. Nan, Y. Sun, Z. Jiang, Three-dimensional porous aerogel constructed by g-C₃N₄ and graphene oxide nanosheets with excellent visible-light photocatalytic performance, ACS Appl. Mater. Interfaces 7 (2015) 25693.

[33] D. Yang, J. Feng, L. Jiang, X. Wu, L. Sheng, Y. Jiang, T. Wei, Z. Fan, Photocatalyst interface engineering: spatially confined growth of ZnFe₂O₄ within graphene networks as excellent visible-light-driven photocatalysts, Adv. Funct. Mater. 25 (2016) 7080–7087.

[34] Z. Yue, A. Liu, C. Zhang, J. Huang, M. Zhu, Y. Du, P. Yang, Noble-metal-free heterostructural CdS/Nb₂O₅/N-doped-graphene ternary photocatalytic system as visible-light- driven photocatalyst for hydrogen evolution, Appl. Catal. B 201 (2017) 202–210.

[35] M. Sun, Y. Wang, Y. Shao, Y. He, Q. Zeng, H. Liang, T. Yan, B. Du, Fabrication of a novel Z-scheme g-C₃N₄/Bi₄O₇ heterojunction photocatalyst with enhanced visible light-driven activity toward organic pollutants, J. Colloid Interface Sci. 501 (2017) 123–132.

[36] H. Wang, W. He, X. Dong, H. Wang, F. Dong, In situ FT-IR investigation on the reaction mechanism of visible light photocatalytic NO oxidation with defective g-C₃N₄, Sci. Bull. 63 (2018) 117–125.

[37] G. Dong, W. Ho, Y. Li, L. Zhang, Facile synthesis of porous graphene-like carbon nitride (C₆N₉H₃) with excellent photocatalytic activity for NO removal, Appl. Catal. B 174–175 (2015) 477–485.

[38] H. Wang, W. Zhang, X. Li, J. Li, W. Cen, Q. Li, F. Dong, Highly enhanced visible light photocatalysis and in situ FT-IR studies on Bi metal@defective BiOCl hierarchical microspheres, Appl. Catal. B 225 (2018) 218–227.

[39] K.I. Hadjiivanov, Identification of neutral and charged NₓOᵧ surface species by IR spectroscopy, Catal. Rev. 42 (2000) 71–144.

[40] W. He, Y. Sun, G. Jiang, H. Huang, X. Zhang, F. Dong, Activation of amorphous Bi₂WO₆ with synchronous Bi metal and Bi₂O₃ coupling: photocatalysis mechanism and reaction pathway, Appl. Catal. B 232 (2018) 340–347.

[41] J. Luo, G. Dong, Y. Zhu, Z. Yang, C. Wang, Switching of semiconducting behavior from n-type to p-type induced high photocatalytic NO removal activity in g-C₃N₄, Appl. Catal. B 214 (2017) 46–56.

[42] Y. Chen, G. Zhu, M. Hojamberdiev, J. Gao, R. Zhu, C. Wang, P. Liu, Three-dimensional Ag₂O/Bi₅O₇I p–n heterojunction photocatalyst harnessing UV–vis–NIR broad spectrum for photodegradation of organic pollutants, J. Hazard. Mater. 344 (2018) 42–54.

[43] Z.F. Huang, J. Song, X. Wang, L. Pan, K. Li, X. Zhang, L. Wang, J.-J. Zou, Switching charge transfer of C₃N₄/W₁₈O₄₉ from type-II to Z-scheme by interfacial band bending for highly efficient photocatalytic hydrogen evolution, Nano Energy 40 (2017) 308–316.

[44] J. Safaei, H. Ullah, N.A. Mohamed, M.F.M. Noh, M.F. Soh, A.A. Tahir, N.A. Ludin, M.A. Ibrahimet, W.N.R.W. Isahak, M.A.M. Teridi, Enhanced photoelectrochemical performance of Z-scheme g-C₃N₄/BiVO₄ photocatalyst, Appl. Catal. B 234 (2018) 296–310.

[45] Y. Gong, X. Quan, H. Yu, S. Chen, Synthesis of Z-scheme Ag₂CrO₄/Ag/g-C₃N₄ composite with enhanced visible-light photocatalytic activity for 2, 4-dichlorophenol degradation, Appl. Catal. B 219 (2017) 439–449.

[46] Y. Huang, Y.X. Gao, Q. Zhang, Y.F. Zhang, J.J. Cao, W.K. Ho, S.C. Lee, Biocompatible FeOOH-carbon quantum dots nanocomposites for gaseous NOₓ removal under visible light: improved charge separation and high selectivity, J. Hazard. Mater. 354 (2018) 54–62.

[47] X. Zeng, Z. Wang, G. Wang, T.R. Gengenbach, D.T. Mccarthy, A. Deletic, J. Yu, X. Zhang, Highly dispersed TiO₂ nanocrystals and WO₃ nanorods on reduced graphene oxide: Z-scheme photocatalysis system for accelerated photocatalytic water disinfection, Appl. Catal. B 218 (2017) 163–173l.

nanocomposites for accelerated photocatalytic water disinfection, Appl. Catal. B 202 (2016) 33–41.